Supporting Information for:

Combined Experimental and Theoretical Investigation on the Magnetic Properties Derived from the Coordination of 6-methyl-2-oxonicotinate to 3d-Metal Ions

Laura Razquin-Bobillo,[a] Oier Pajuelo-Corral,[a] Beñat Artetxe,[b] Andoni Zabala-Lekuona,[a] Duane Choquesillo-Lazarte,[c] Antonio Rodríguez-Diéguez,[c] Eider San Sebastian,[a] Javier Cepeda*,[a]

[a] Departamento de Química Aplicada, Facultad de Química, Universidad del País Vasco/Euskal Herriko Unibertsitatea (UPV/EHU), 20018 Donostia-San Sebastián, Spain. [b] Departamento de Química Orgánica e Inorgánica, Facultad de Ciencia y Tecnología, Universidad del País Vasco/Euskal Herriko Unibertsitatea (UPV/EHU), 48940, Leioa, Spain. [c] Laboratorio de Estudios Cristalográficos, IACT, CSIC-Universidad de Granada, Avda. de las Palmeras 4, 18100 Armilla, Spain. [d] Departamento de Química Inorgánica, Facultad de Ciencias, Universidad de Granada, 18071 Granada, Spain.

Contents:

S1. Chemical and thermal characterization of compounds.

The thermal behaviour of all compounds has been studied by means of thermogravimetric/differential thermal analyses (TG/DTA) in order to further confirm the purity of the polycrystalline samples. As it can be seen in the TG curves (see Table S1), when the compounds are heated above room temperature, they show a loss of mass that is assigned to the solvent molecules in good agreement with the amount of solvent molecules found in X ray diffraction analyses. Above 300 °C, compounds $\mathbf{1}_{Mn}$ and $\mathbf{5}_{Cu}$ undergo one exothermic process each whereas two exothermic processes can be distinguished for compounds $\mathbf{2}_{Co}$, $\mathbf{3}_{Ni}$ and $\mathbf{4}_{Cu}$ as a consequence of the combustion of the organic molecules. The final residues agree well with the mass percentage expected for the oxides of the metal ions of which they are composed.

Table S1. DTA curves of compounds $\mathbf{1_{Mn}}$-$\mathbf{5_{Cu}}$.

{[MnNa(μ3-6m2onic)2(μ-6m2onic)(MeOH)]·H2O·MeOH}n (1Mn)

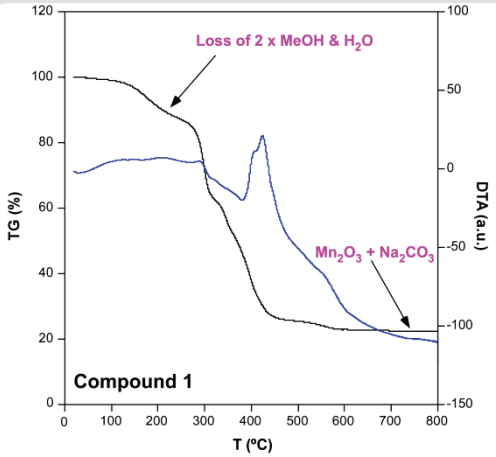

{[Co2Na2(μ3-6m2onic)2(μ-6m2onic)2(μ-H2O)(H2O)6](NO3)2}n (2Co)

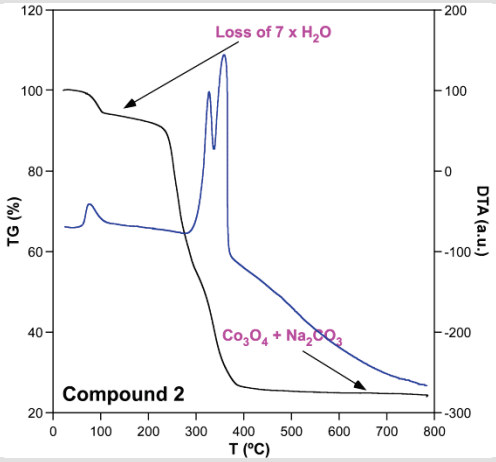

{[Ni2Na2(μ3-6m2onic)2(μ-6m2onic)2(μ-H2O)(H2O)6](NO3)2}n (3Ni)

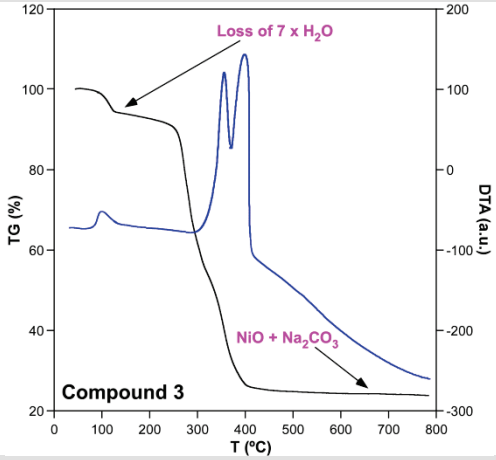

{2[Cu2(6m2onic)3(μ-6m2onic)3(MeOH)]·[Cu2(6m2onic)2(μ-6m2onic)2]·2[Cu(6m2onic)2(MeOH)]·32H2O}n (4Cu)

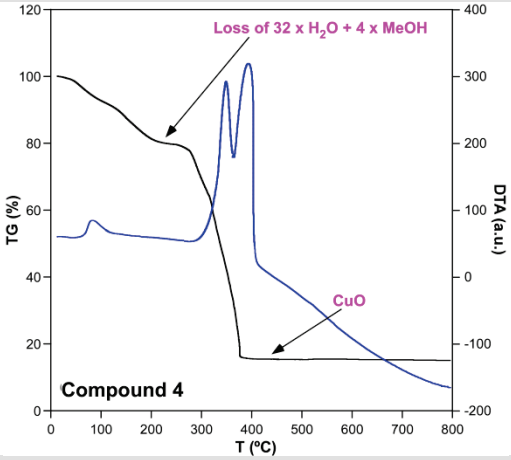

{[Cu(μ-6m2onic)2]·6H2O}n (5Cu)

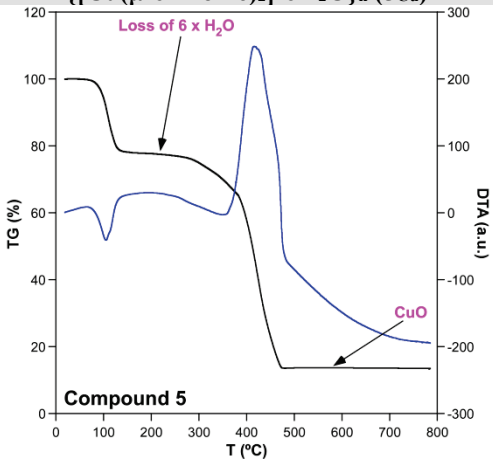

S2. FT-IR spectroscopy

Infrared spectroscopy has been used for the initial characterisation of the compounds, as it reveals the presence of ligand copies in the synthesised complexes, as well as its coordination to metal, if any. The spectra obtained for complexes **1$_{Mn}$-5$_{Cu}$** show a similar pattern (Figure S1), which can be considered as the result of the ligand exhibiting the same tautomeric form in all compounds. In this regard, it should be mentioned that although the coordination mode of the 1H-2-oxo-6-methyl-nicotinate tautomer may be variable, compounds **1$_{Mn}$-5$_{Cu}$** all show signals corresponding to a chelate ring between the ketone and carboxylate groups, imposing the main similarity of the infrared spectra (presence of most of the bands).

In all the spectra, the first band appearing between 3500-3300 cm^{-1} corresponds to the vibrational stress of the O-H bonds of the adsorbed water molecules in the samples by the environmental humidity (in the case of the free ligand) or of the crystallization water molecules (in the case of the compounds). This band is followed by a second, broader band between 3300-2300 cm^{-1}, which corresponds to the vibrations of the O-H, N-H and C-H bonds of the ligand. It is significant that in the ligand spectrum this band is much more intense than with the compounds, as the inter- and intra-molecular hydrogen bonds between the ligand molecules vibrate more intensely. In particular, a broad band of the protonated carboxylate group is seen in the ligand and weak vibrational signals of the N-H and C-H pyridine ring are observed in all compounds. The sharp and strong bands appearing in the range 1725-1450 cm^{-1} correspond to asymmetric vibrations of the carboxylate group and the C-C and C-N bonds of the aromatic ring, while the symmetric vibrations of the carboxylate group appear in the range 1400-1200 cm^{-1}. Again, the spectrum of the free ligand shows a strong broad band between 1725-1665 cm^{-1} and narrower at 1508 cm^{-1}, an event that corresponds to the protonation of the carboxylate group. It should also be noted that some symmetric vibrations of the carboxylate group are rather impeded in the compounds by the coordination form adopted in the compounds. The remaining bands of smaller wavenumbers can be assigned to the distortions occurring in the aromatic ring, among which M-O bonds (M = Mn, Co, Ni, Cu) are also seen.

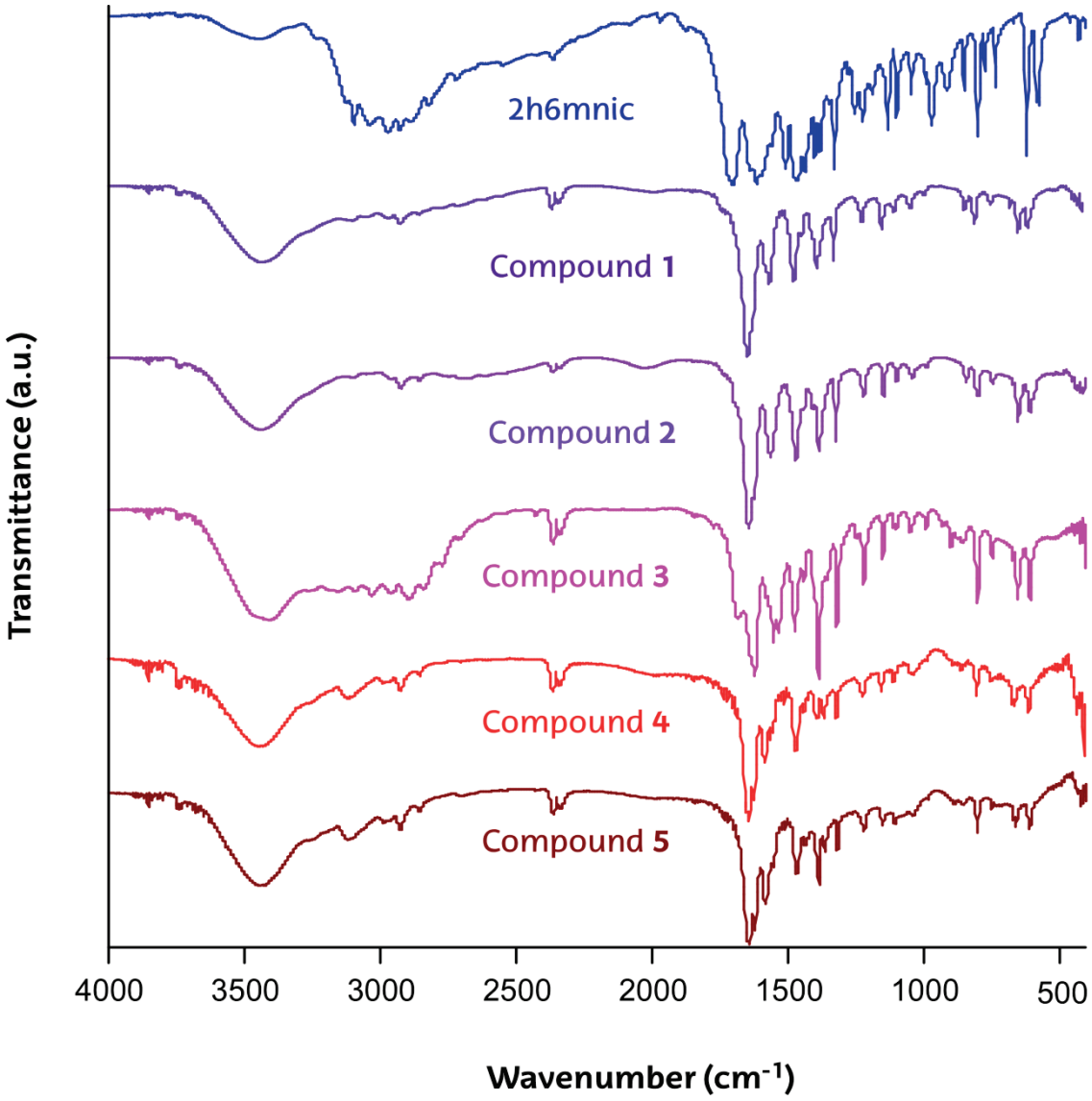

Figure S1. IR spectra of H2h6mnic ligand and compounds $\mathbf{1}_{Mn}$-$\mathbf{5}_{Cu}$.

S3. Powder X-ray diffraction analysis of as-synthesized compounds.

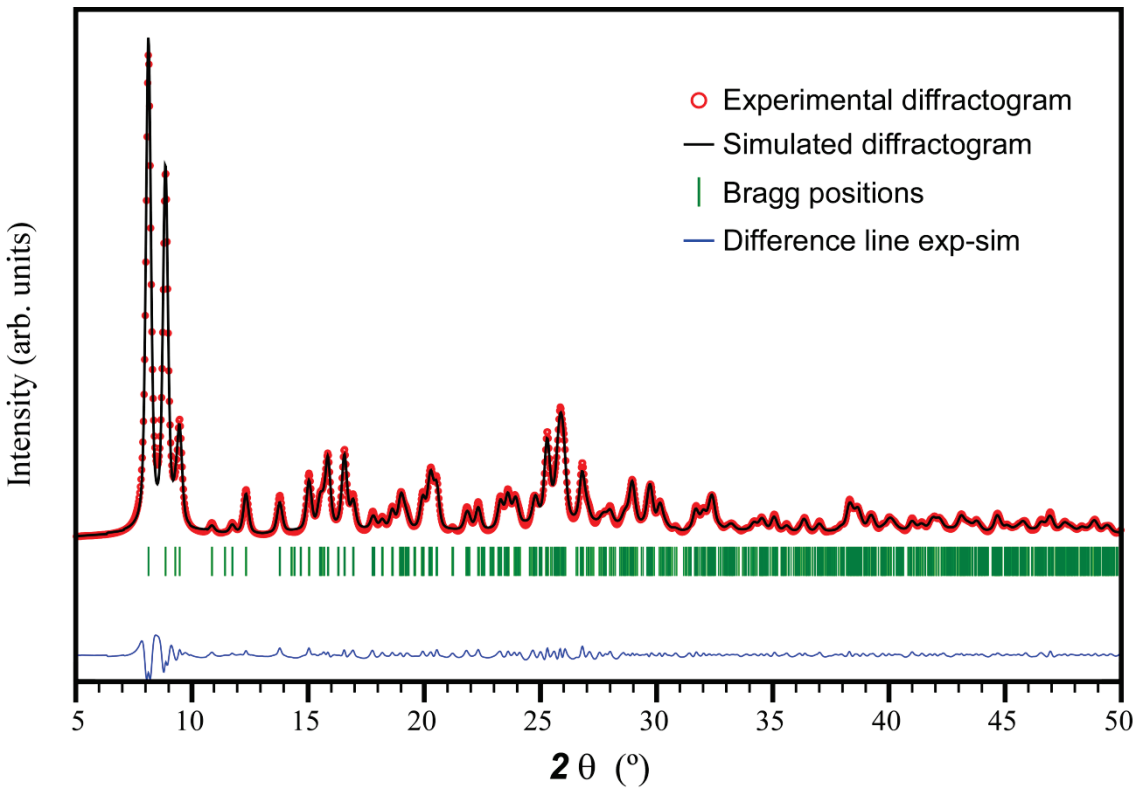

Figure S2. Simulated and experimental PXRD of $\mathbf{1_{Mn}}$ with the full profile pattern matching analyses.

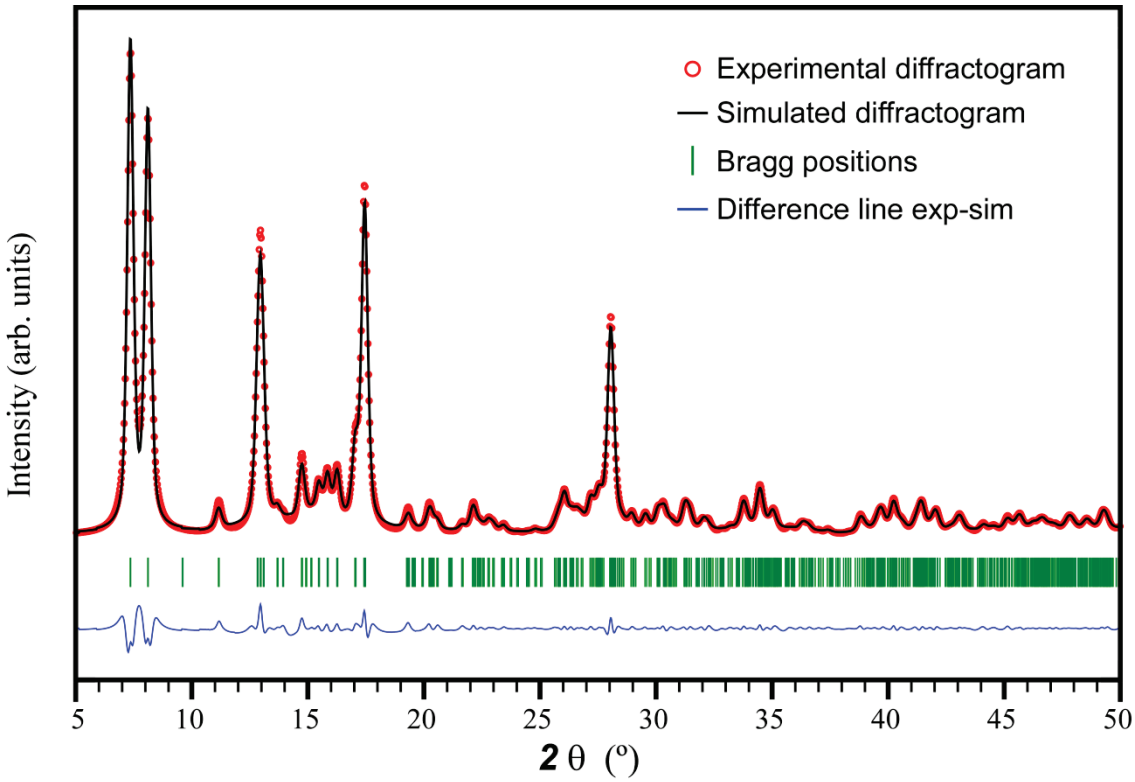

Figure S3. Simulated and experimental PXRD of $\mathbf{2_{Co}}$ with the full profile pattern matching analyses.

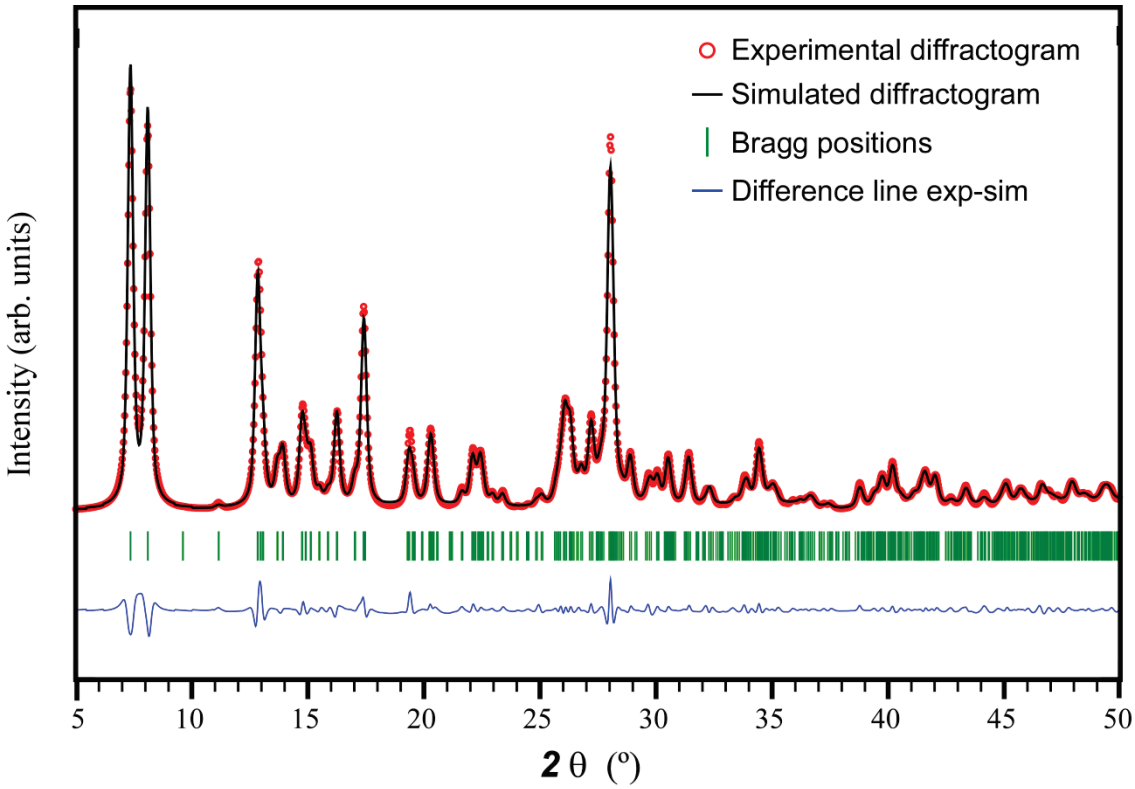

Figure S4. Simulated and experimental PXRD of $\mathbf{3_{Ni}}$ with the full profile pattern matching analyses.

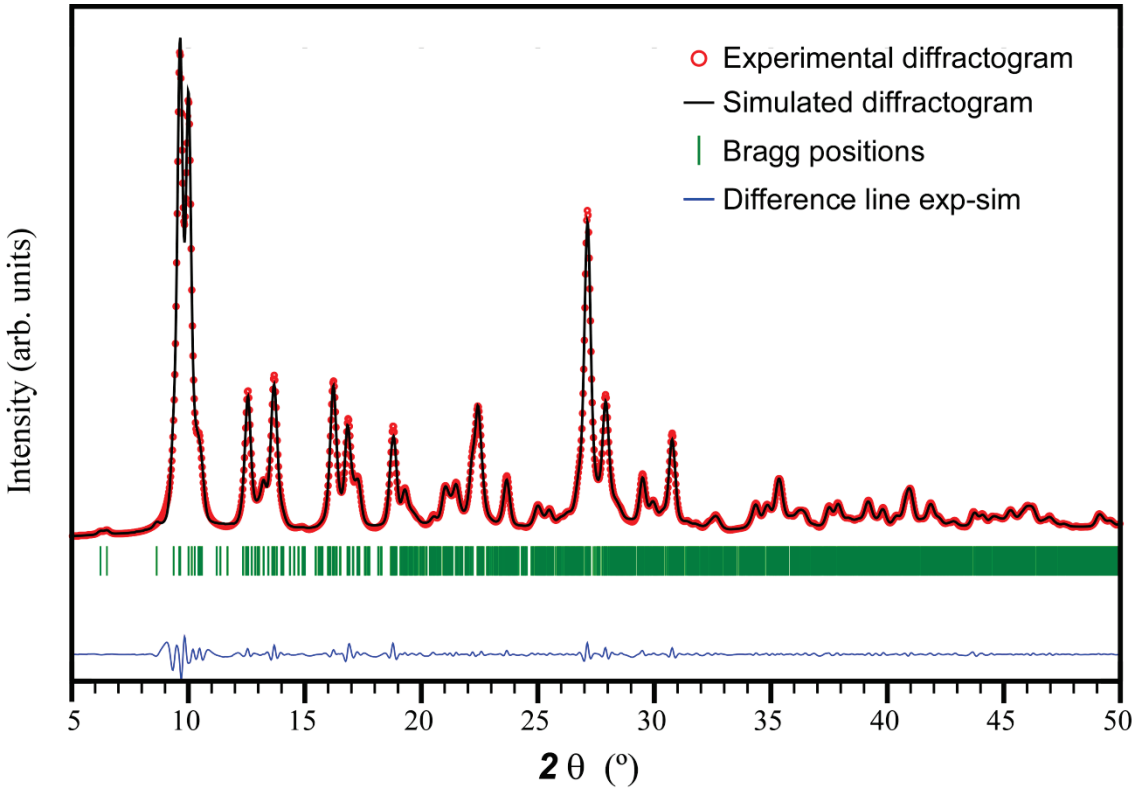

Figure S5. Simulated and experimental PXRD of $\mathbf{4_{Cu}}$ with the full profile pattern matching analyses.

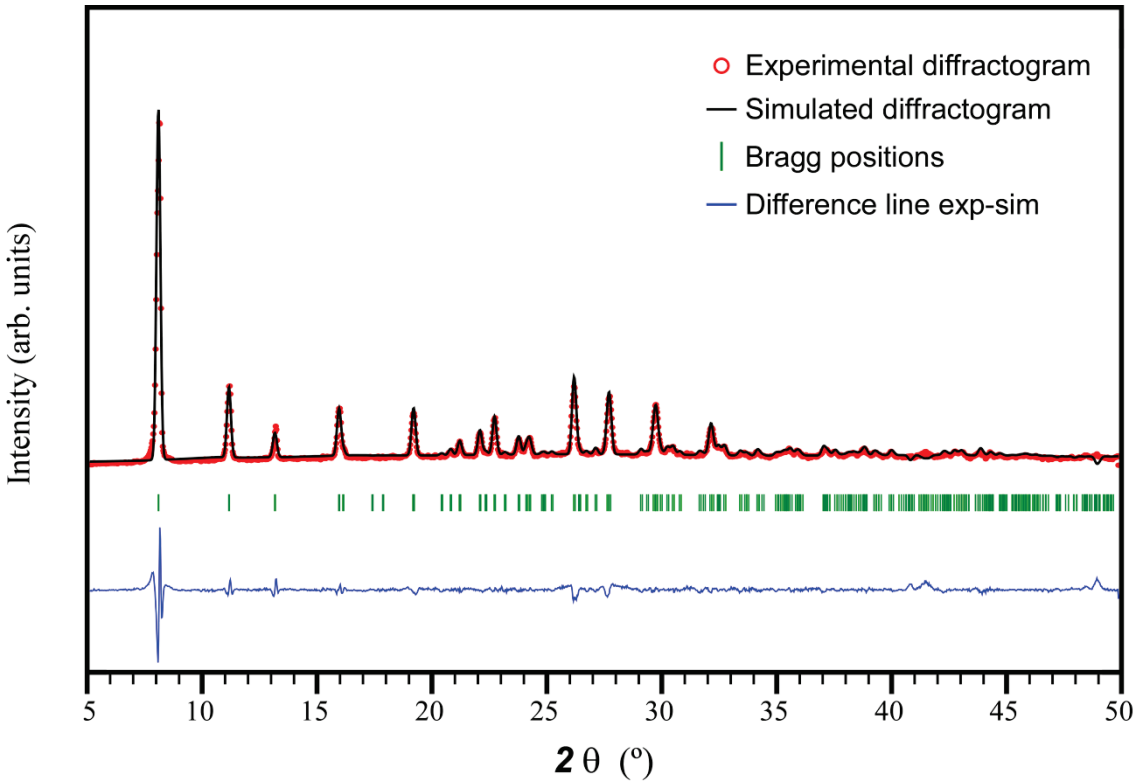

Figure S6. Simulated and experimental PXRD of $\mathbf{5_{Cu}}$ with the full profile pattern matching analyses.

S4. Structural details of compounds $\mathbf{1}_{Mn}$-$\mathbf{5}_{Cu}$

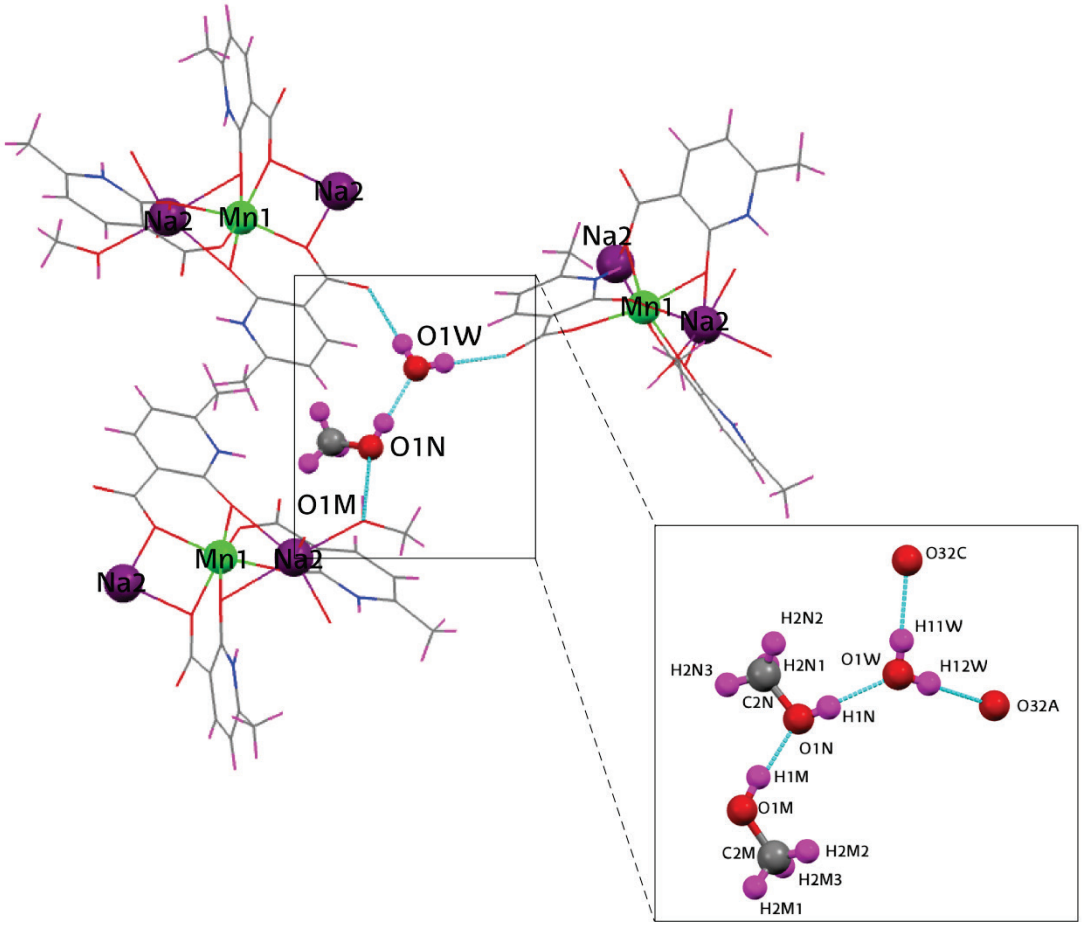

Figure S7. View of the hydrogen bonds formed between the chains of compound $\mathbf{1}_{Mn}$. Inset: Atom numbered solvent and ligand molecules participating in the H-bond network.

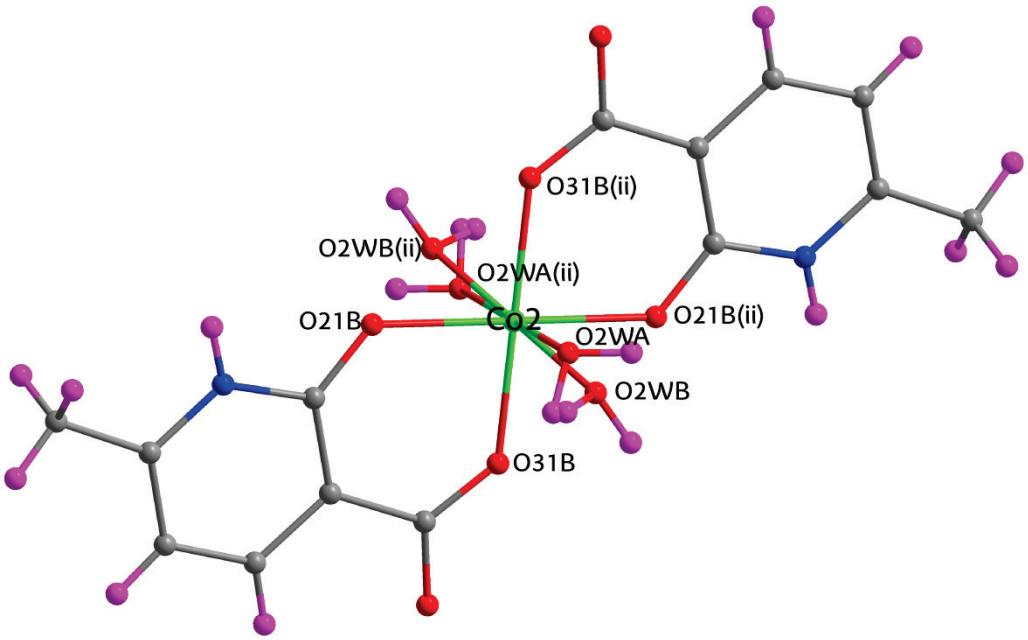

Figure S8. View of the disorder of the molecules O2wA and O2wB for Co2 atom.

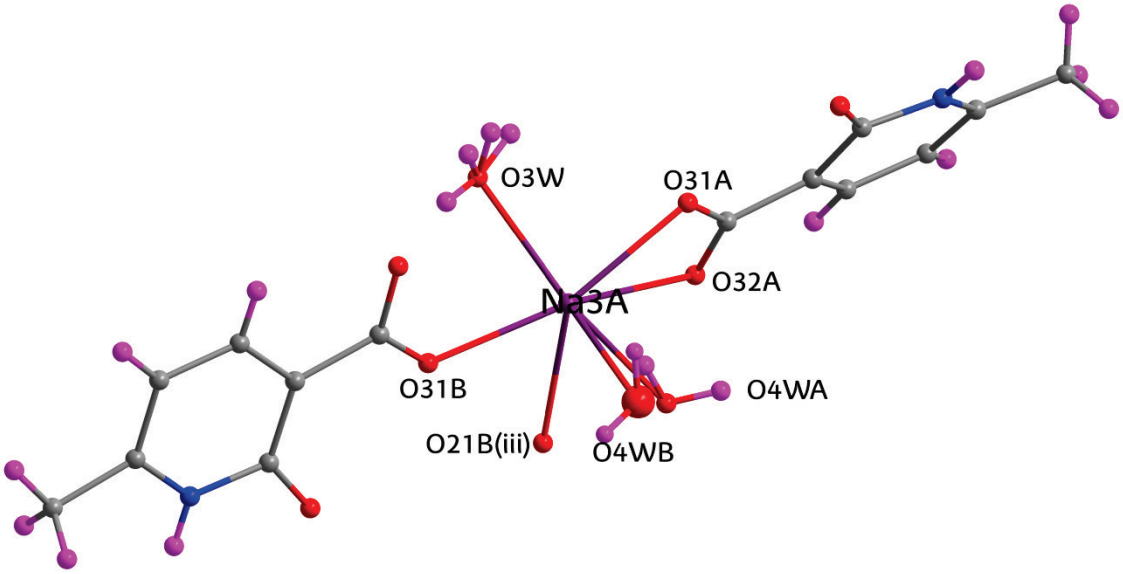

Figure S9. View of the disorder of the molecules O4wA and O4wB for Na3A atom.

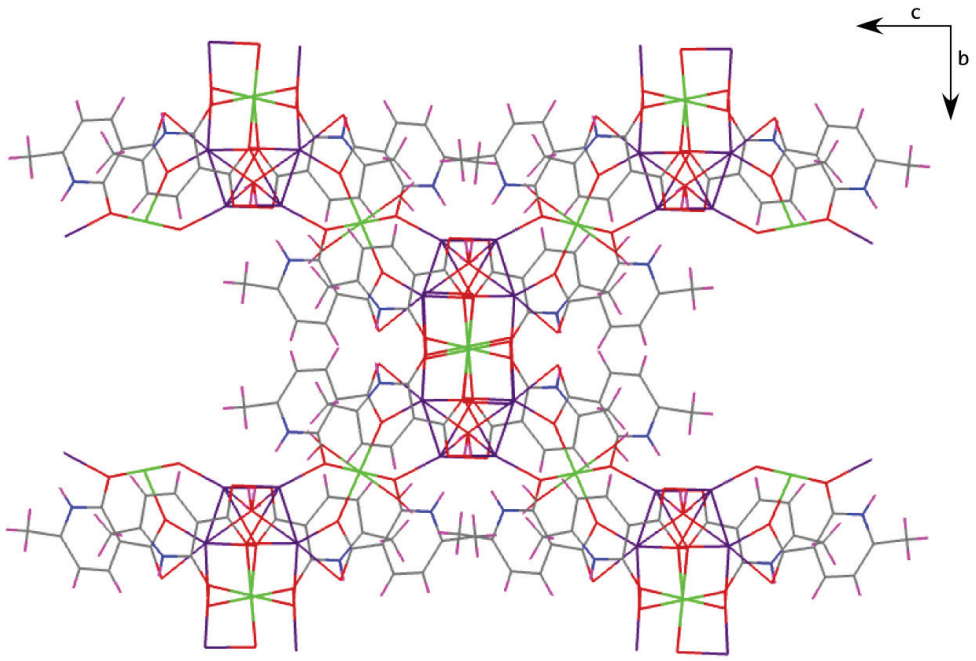

Figure S10. View of the 3D network of $\mathbf{2}_{\mathbf{Co}}$ along crystallographic *a* axis. Nitrate anions have been omitted for clarity.

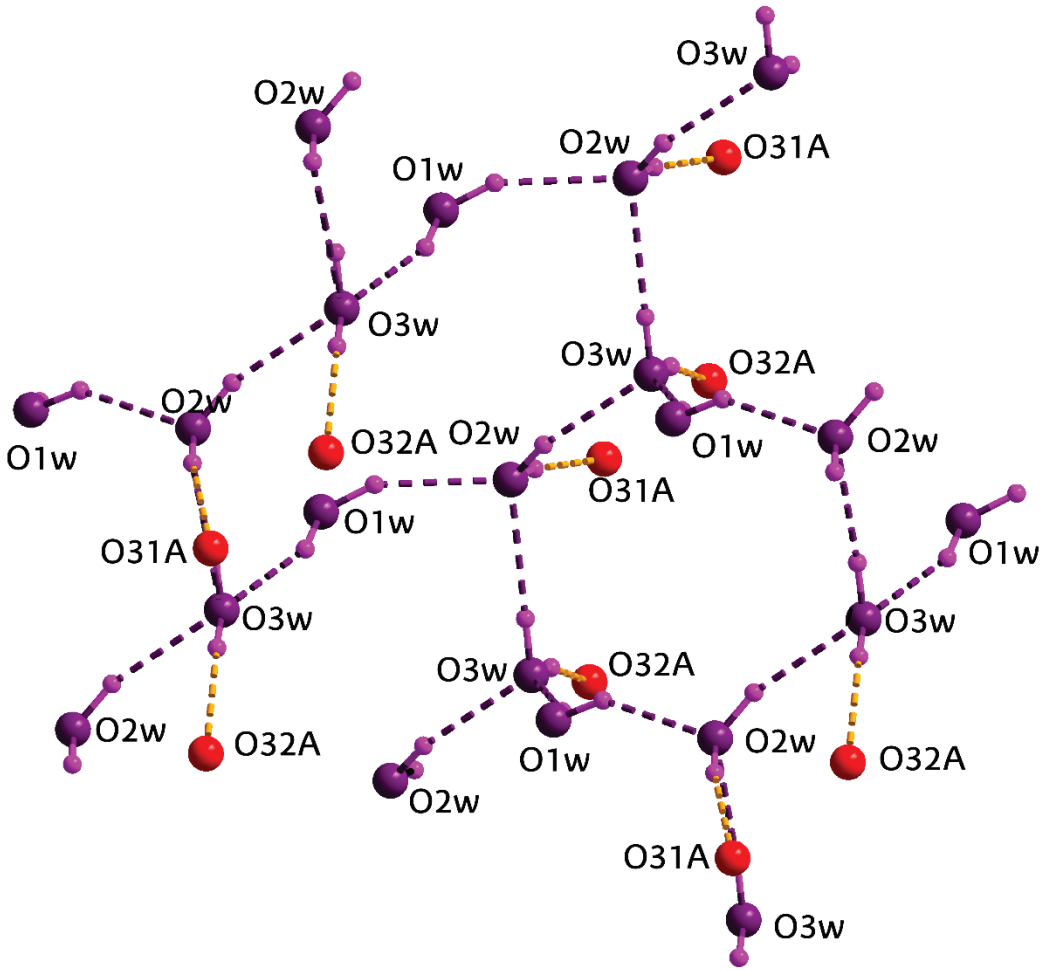

Figure S11. View of the hydrogen bonded water clusters crystallised in compound $\mathbf{5}_{Cu}$.

S5. Continuous Shape Measurements (CShMs).

Table S2. CShMs for the coordination environment of compounds $\mathbf{1_{Mn}}$, $\mathbf{2_{Co}}$, $\mathbf{4_{Cu}}$ and $\mathbf{5_{Cu}}$. The lowest values for each ion are shown in bold to indicate best fits.

Codes:

HP-6	1 D6h	Hexagon
PPY-6	2 C5v	Pentagonal pyramid
OC-6	3 Oh	Octahedron
TPR-6	4 D3h	Trigonal prism
JPPY-6	5 C5v	Johnson pentagonal pyramid J12

Structure [ML6]	HP-6	PPY-6	OC-6	TPR-6	JPPY-6
1_{Mn} (Mn1)	33.126	20.671	**2.565**	7.208	24.521
1_{Mn} (Na2)	29.682	20.917	**4.380**	8.842	24.496
2_{Co} (Co1)	31.922	29.364	**0.129**	16.295	32.571
2_{Co} (Co2)	30.222	28.640	**0.278**	16.174	31.743
2_{Co} (Na3A)	47.382	**29.034**	38.934	34.949	32.934
5_{Cu} (Cu1)	31.212	28.910	**2.708**	18.400	31.074

Codes:

PP-5	1 D5h	Pentagon
vOC-5	2 C4v	Vacant octahedron
TBPY-5	3 D3h	Trigonal bipyramid
SPY-5	4 C4v	Spherical square pyramid
JTBPY-5	5 D3h	Johnson trigonal pyramid J12

Structure [ML5]	PP-5	vOC-5	TBPY-5	SPY-5	JTBPY-5
4_{Cu} (Cu1)	30.483	1.276	5.404	**1.039**	8.364
4_{Cu} (Cu2)	32.396	1.634	5.614	**0.786**	8.806
4_{Cu} (Cu3)	30.300	1.189	5.512	**0.917**	8.466
4_{Cu} (Cu4)	32.959	1.438	4.827	**0.638**	8.024

S6. Diffuse reflectance results

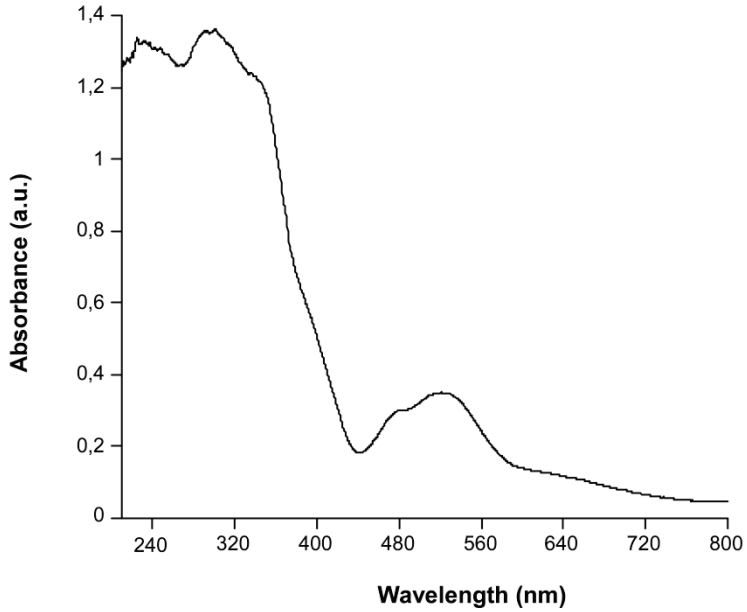

Figure S12. Diffuse reflectance spectrum for compound $\mathbf{2}_{Co}$.

S7. DC magnetic susceptibility measurements

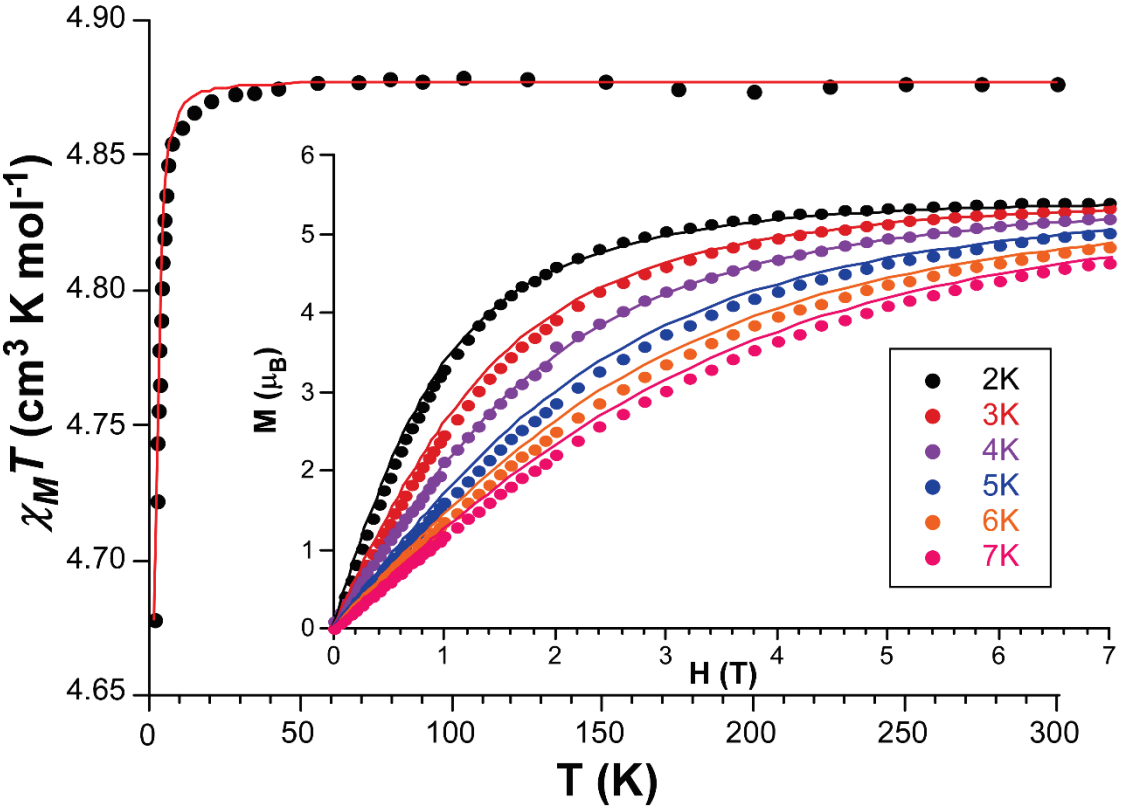

Figure S13. $\chi_M T$ *vs* T and variable-temperature magnetization plots for $\mathbf{1_{Mn}}$ showing the best fit according to eq.1.

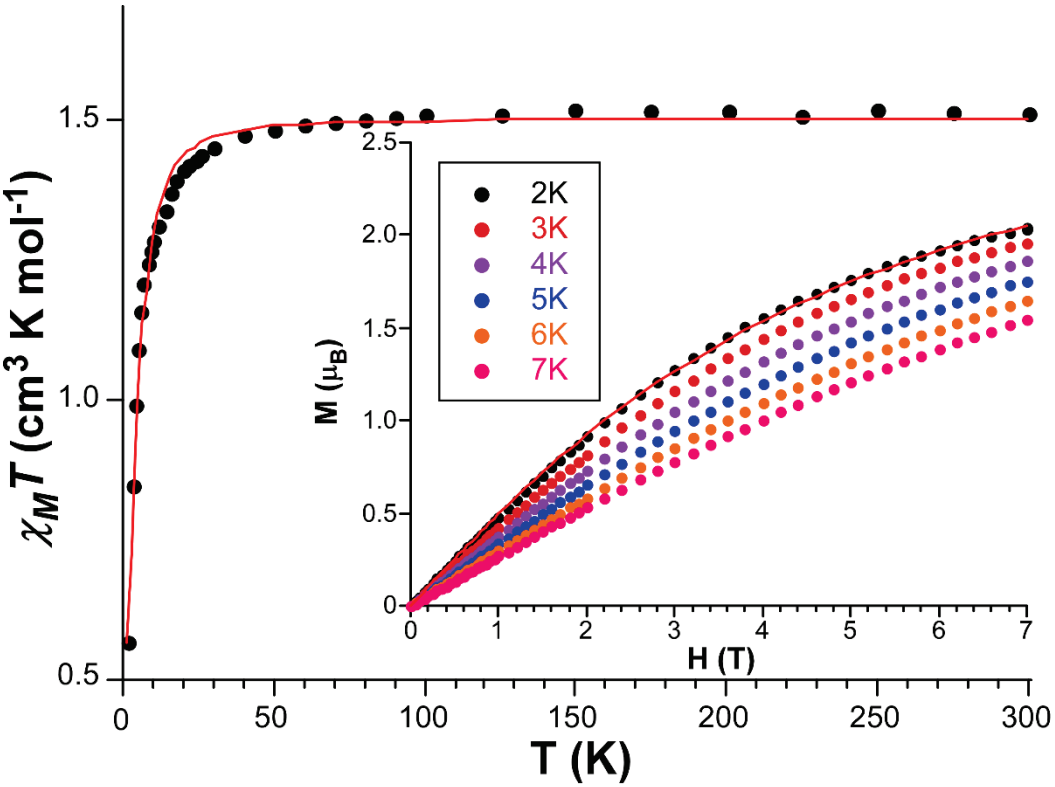

Figure S14. $\chi_M T$ *vs* T and variable-temperature magnetization plots for $\mathbf{3_{Ni}}$ showing the best fit according to eq.1.

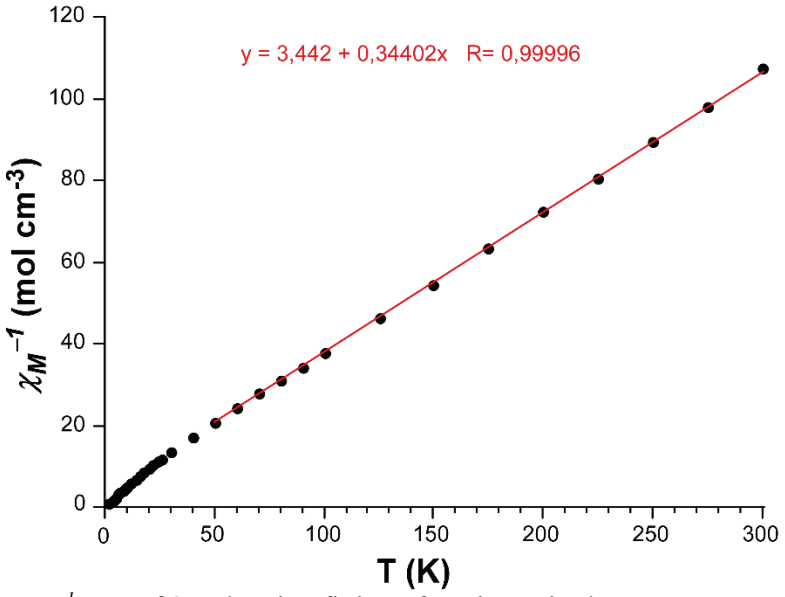

Figure S15. χ_M^{-1} *vs T* of $\mathbf{2_{Co}}$ showing fitting of Curie-Weiss law.

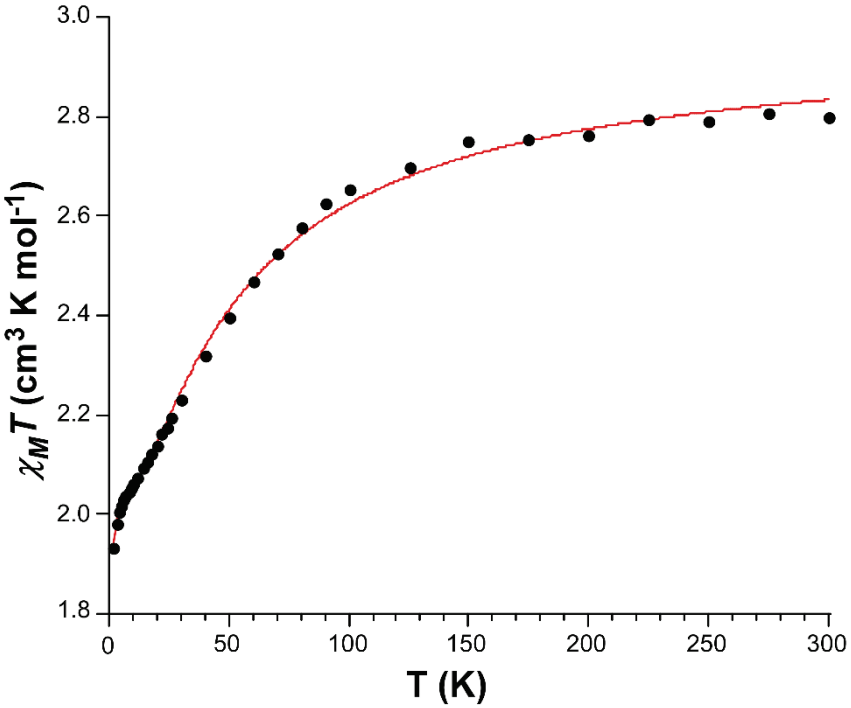

Figure S16. $\chi_M T$ *vs T* plots of $\mathbf{2_{Co}}$ showing the best fit according to eq.3.

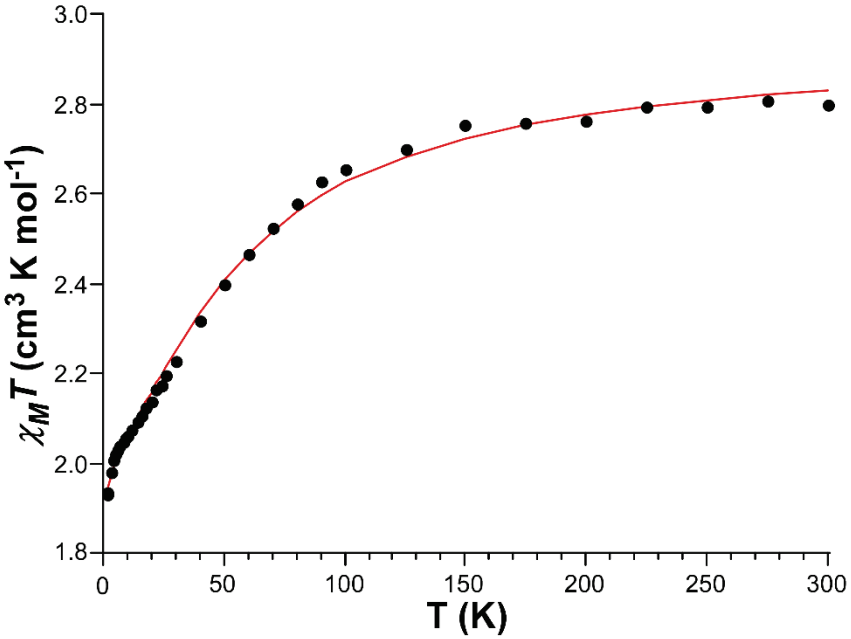

Figure S17. $\chi_M T$ *vs* T plots of $\mathbf{2_{Co}}$ showing the best fit according to eq.4 in an octahedral geometry.

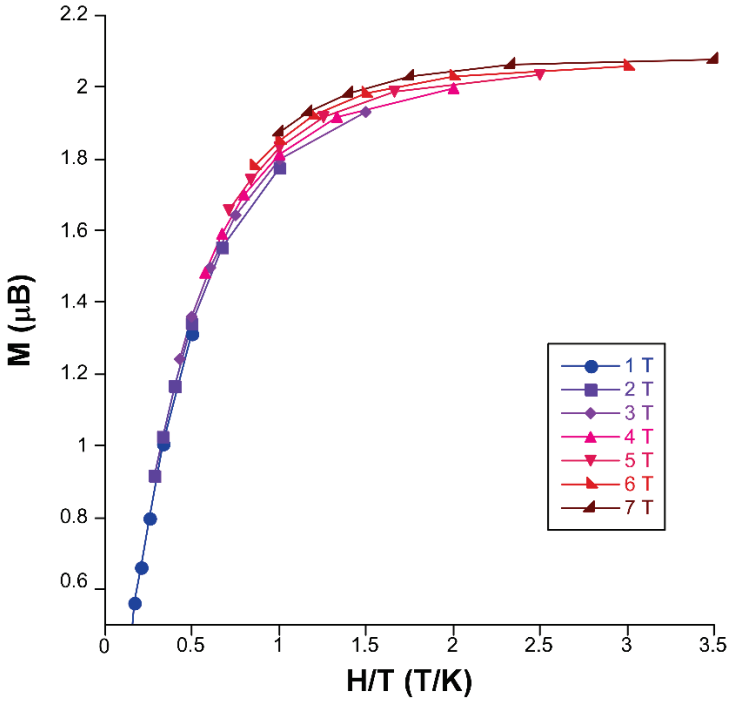

Figure S18. Reduced magnetization curves in the 2-7 K and 1-7 T region for compound $\mathbf{2_{Co}}$.

S8. AC magnetic susceptibility measurements

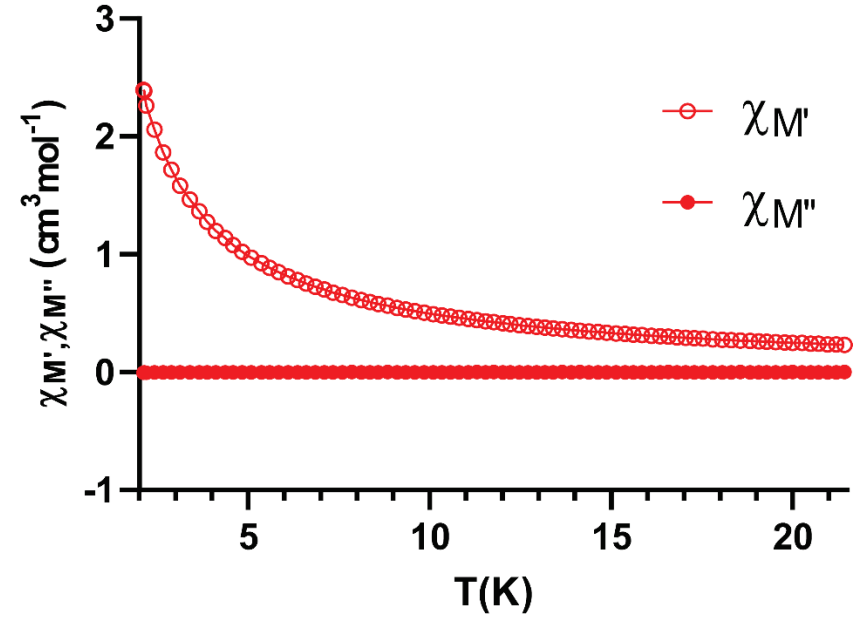

Figure S19. χ_M' and χ_M'' vs T plots under H_{dc} = 0 Oe and H_{ac} = 3.5 Oe (frequency of 10000 Hz) for compound $\mathbf{1_{Mn}}$.

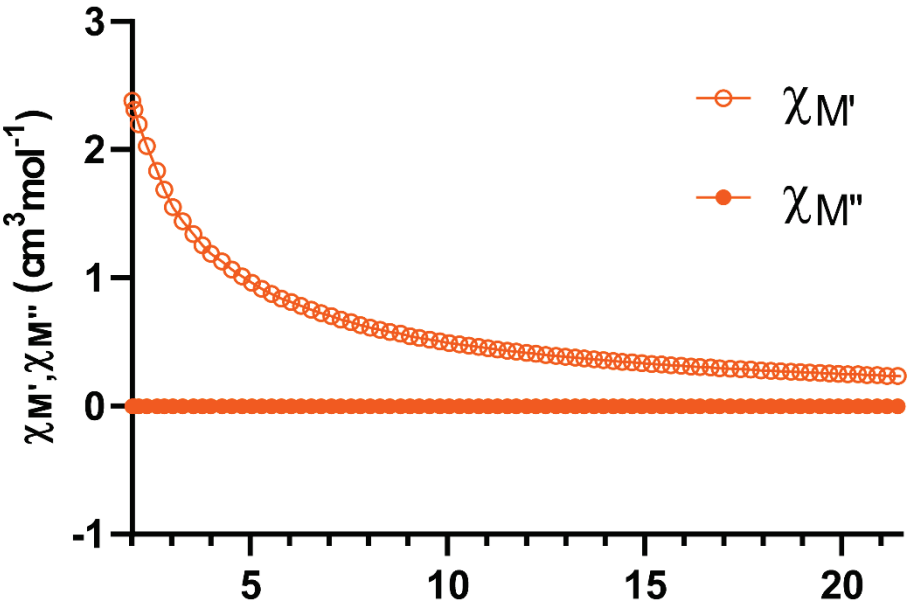

Figure S20. χ_M' and χ_M'' vs T plots under H_{dc} = 1000 Oe and H_{ac} = 3.5 Oe (frequency of 10000 Hz) for compound $\mathbf{1_{Mn}}$.

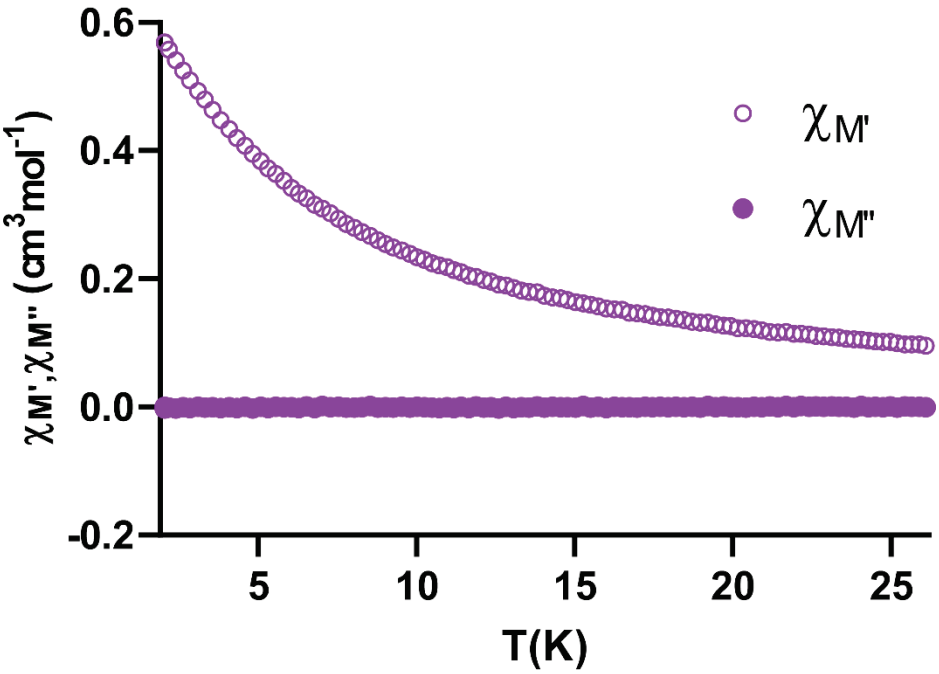

Figure S21. χ_M' and χ_M'' vs T plots under H_{dc} = 0 Oe and H_{ac} = 3.5 Oe (frequency of 10000 Hz) for compound $\mathbf{3_{Ni}}$.

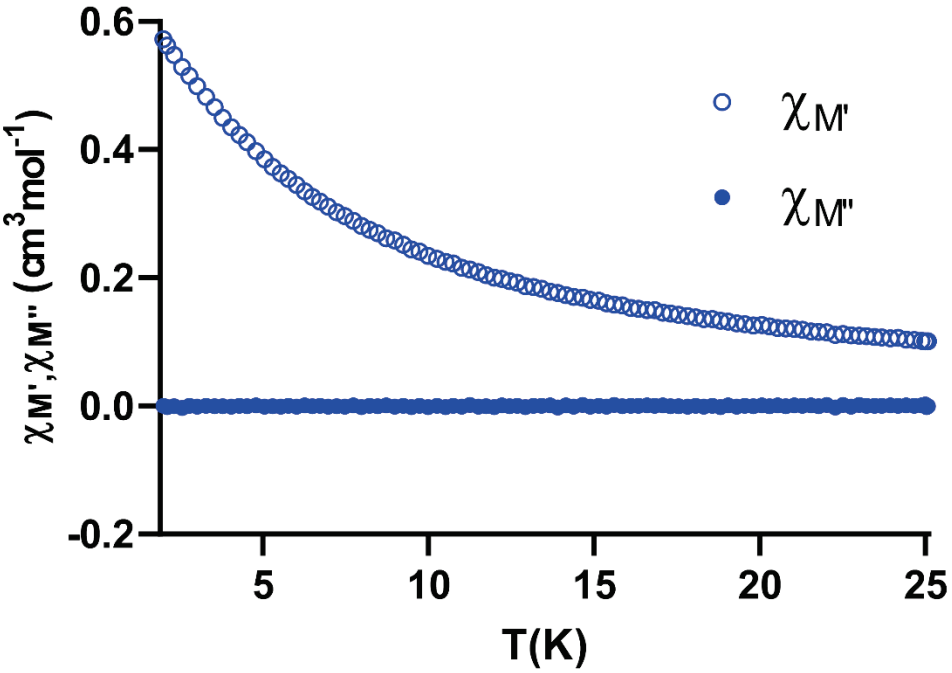

Figure S22. χ_M' and χ_M'' vs T plots under H_{dc} = 1000 Oe and H_{ac} = 3.5 Oe (frequency of 10000 Hz) for compound $\mathbf{3_{Ni}}$.

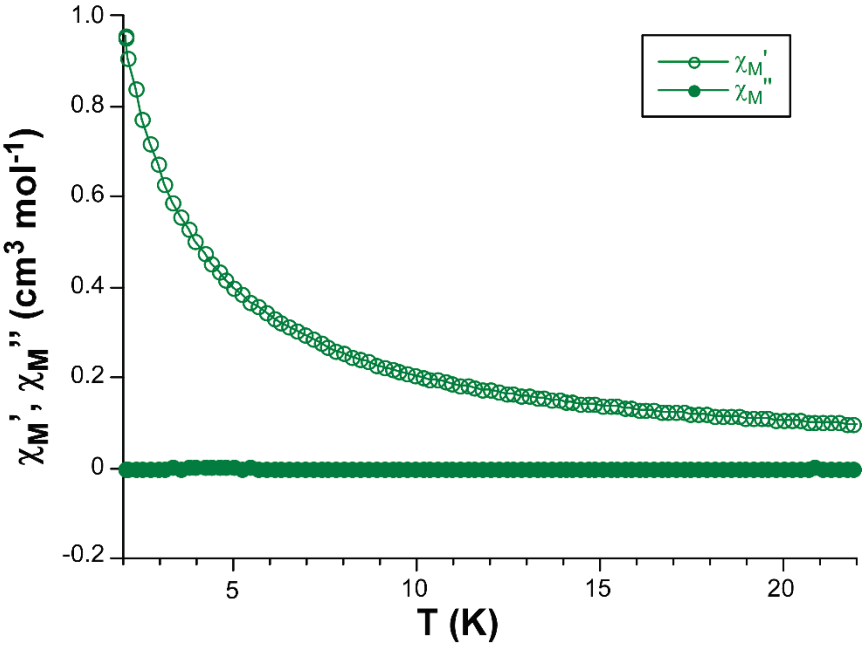

Figure S23. χ_M' and χ_M'' vs T plots under H_{dc} = 0 Oe and H_{ac} = 3.5 Oe (frequency of 10000 Hz) for compound $\mathbf{2}_{Co}$.

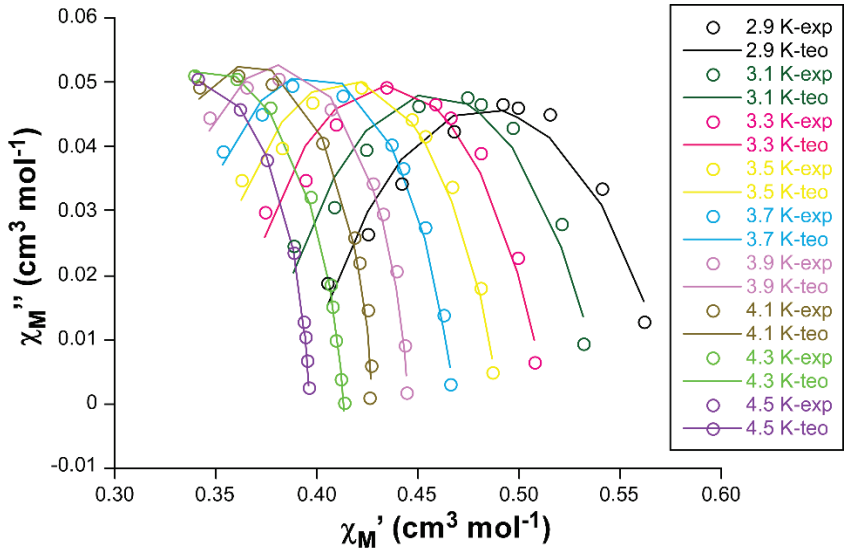

Figure S24. Cole-Cole plot for compound $\mathbf{2}_{Co}$ in the 2.9–4.5 K range.

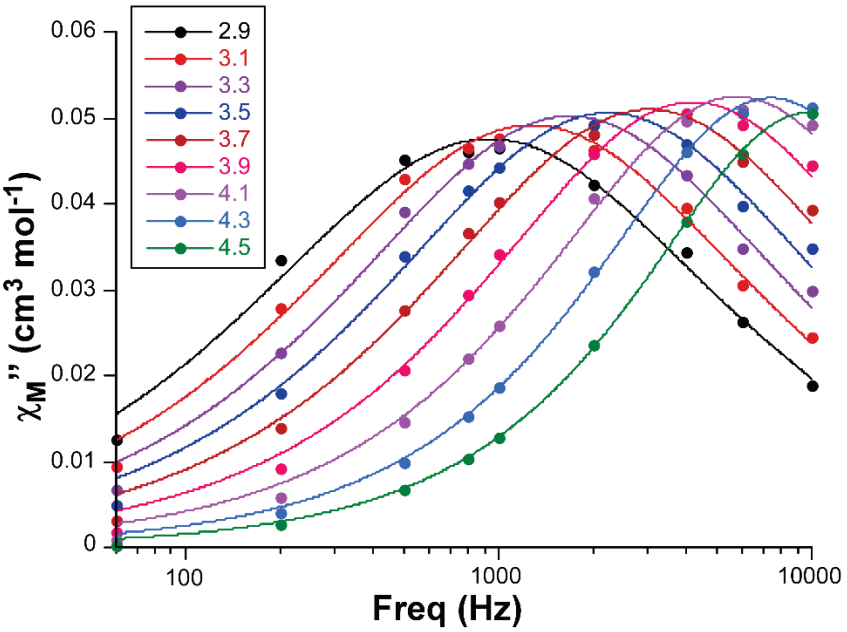

Figure S25. Variable-temperature frequency dependence of the χ_M'' signal of $\mathbf{2_{Co}}$ in the 2.9–4.5 K range showing the best fitting.

S9. CASSCF multiconfigurational calculations.

Table S3. Ab initio calculated low-lying spin-orbit energy states (cm^{-1}) for the two independent Co(II) atoms of $\mathbf{2_{Co}}$.

Co1	Co2
0.00	0.00
0.00	0.00
198.08	245.96
198.08	245.96
765.78	579.63
765.78	579.63
1052.00	918.11
1052.00	918.11
1429.66	1293.86
1429.66	1293.86
1514.24	1358.92
1514.24	1358.92

Table S4. NEVPT2 results calculated on the H-optimized structure grown around Co2 atom of compound $\mathbf{2_{Co}}$.[a]

D (D_{KD1-2}, D_{KD1-3})[b]	+101.7 (+59.7, +26.6)
E/D	0.33
g_{xx}, g_{yy}, g_{zz}	1.76, 2.32, 3.09
g_{iso}	2.39
ΔE (1-2), ΔE (1-3) [c]	245.9, 579.6

[a] Energy values are given in cm^{-1}. [b] The two values in parentheses after D represent the contribution to D of the ground to first and ground to second exited state transitions, respectively. [c] Energy separation between KDs.

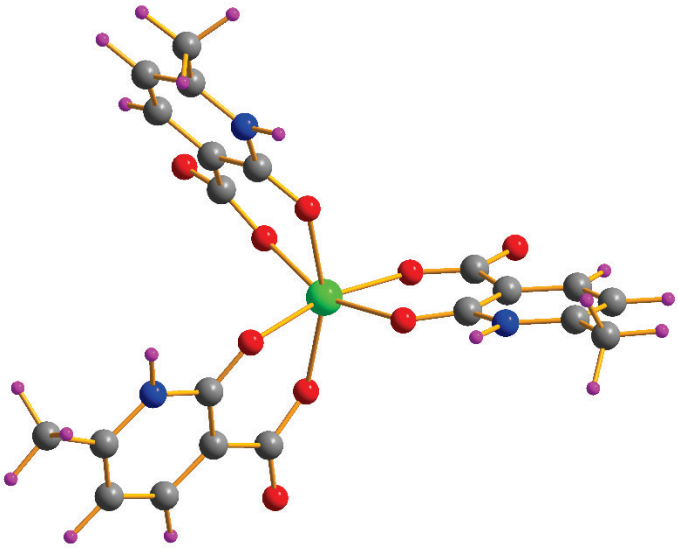

Figure S26. Model of $\mathbf{1_{Mn}}$ used for ab initio calculations.

Table S5. Calculated CAS(5,5)/NEVPT2 transition energies results calculated on the H-optimized model of compound $\mathbf{1_{Mn}}$.[a]

Root	***Multiplicity***	***ΔE (cm^{-1})***
0	4	20289
1	4	20989
2	4	21541
3	4	24600
4	4	24935
5	4	25055
6	4	26368
7	4	26382
8	4	26535
0	2	28369
1	2	28571
2	2	29586
9	4	29785
10	4	29994

Table S6. NEVPT2 results calculated on the H-optimized model of compound $\mathbf{1_{Mn}}$.[a]

D **(*D*$_{KD1-2}$, *D*$_{KD1-3}$)[b]**	-0.04 (-0.40, -0.36)
E*/*D	0.31
g_{xx}, g_{yy}, g_{zz}	2.00, 2.00, 2.00
g_{iso}	2.00
ΔE (1-2), ΔE (1-3)[c]	0.098, 0.173

[a] Energy values are given in cm^{-1}. [b] The two values in parentheses after *D* represent the contribution to *D* of the ground to first and ground to second exited state transitions, respectively. [c] Energy separation between KDs.

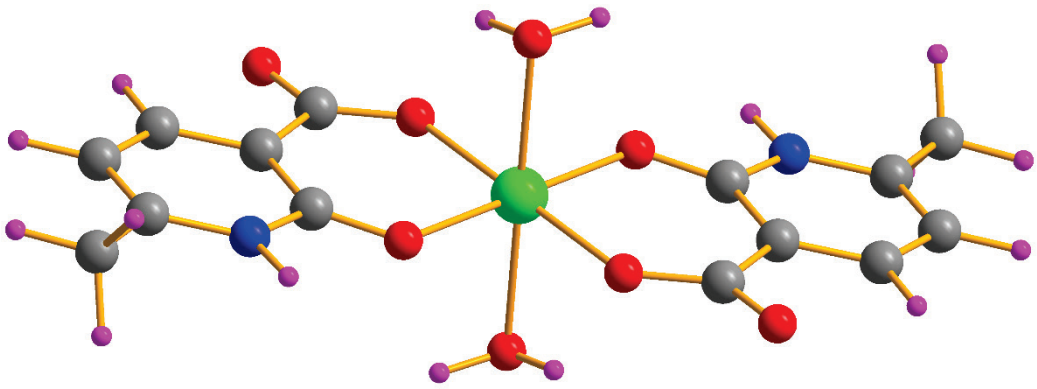

Figure S27. Model of $\mathbf{3_{Ni}}$ used for ab initio calculations.

Table S7. Calculated CAS(8,5)/NEVPT2 transition energies results calculated on the H-optimized model of compound $\mathbf{3_{Ni}}$.[a]

Root	***Multiplicity***	$\Delta E\ (cm^{-1})$
1	3	7155
2	3	7401
3	3	9837
4	3	13100
5	3	14220
0	1	14708
6	3	15838
1	1	16207
2	1	22475
3	1	22957
7	3	24835
4	1	25211
8	3	26568
5	1	27309
6	1	27786
9	3	28259

Table S8. NEVPT2 results calculated on the H-optimized model of compound $\mathbf{3_{Ni}}$.[a]

$\boldsymbol{D}$ **(**$\boldsymbol{D_{KD1\text{-}2}}$**,** $\boldsymbol{D_{KD1\text{-}3}}$**)**[b]	+14.4 (+33.5, +36.9)
$\boldsymbol{E/D}$	0.28
$\boldsymbol{g_{xx}}$**,** $\boldsymbol{g_{yy}}$**,** $\boldsymbol{g_{zz}}$	2.29, 2.37, 2.43
$\boldsymbol{g_{iso}}$	2.36
ΔE (1-2), ΔE (1-3) [c]	5.19, 18.36

[a] Energy values are given in cm^{-1}. [b] The two values in parentheses after *D* represent the contribution to *D* of the ground to first and ground to second exited state transitions, respectively. [c] Energy separation between lowest-lying spin-orbit states.

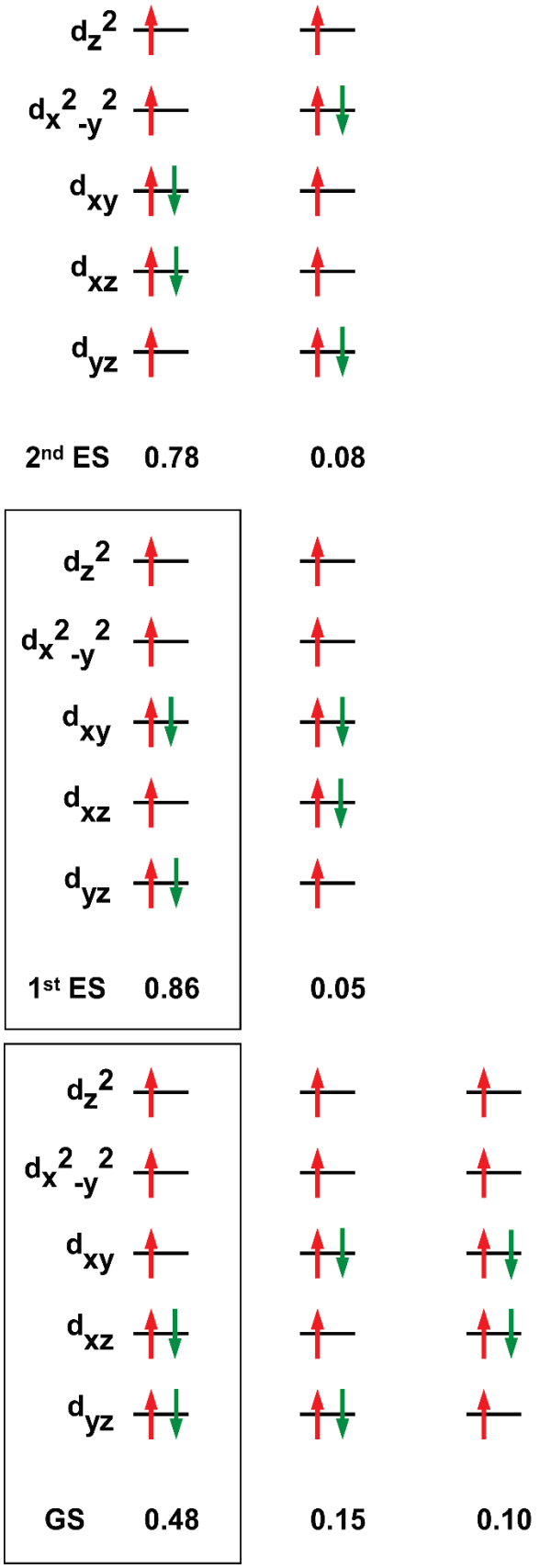

Figure S28. Multiconfigurational analysis of the lowest-lying states of compound $\mathbf{2}_{Co}$ from CASSCF calculation.

S10. DFT calculations.

DFT calculations were conducted on the two tautomeric forms of the ligand to inspect their relative stability.

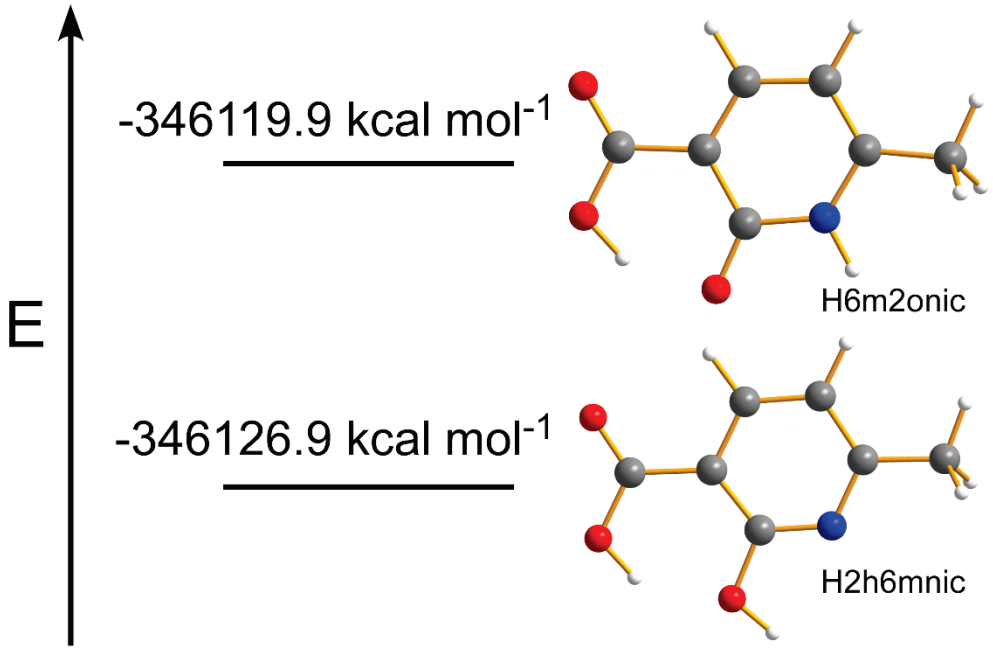

Figure S29. Enthalpies of the two tautomeric forms of the ligand molecule.

S10. References

1 A. EARNSHAW, ed. A. B. T.-I. to M. EARNSHAW, Academic Press, 1968, pp. ix–x.
2 Bruker, *APEX2*, Madison, Wisconsin, USA, 2012.
3 G. M. Sheldrick, *SADABS empirical absorption program*, 1996.
4 G. M. Sheldrick, *Acta Crystallogr. Sect. A*, 2015, **71**, 3–8.
5 G. M. Sheldrick, *Acta Crystallogr. Sect. C*, 2015, **71**, 3–8.
6 G. M. Sheldrick, *Acta Cryst.*, 2014, 3–8.
7 L. J. Farrugia, *J. Appl. Crystallogr.*, 2012, **45**, 849–854.
8 J. Rodríguez-Carvajal, *Phys. B Condens. Matter*, 1993, **192**, 55–69.